JOURNAL OF THERMOPHYSICS AND HEAT TRANSFER
Vol. 17, No. 2, April–June 2003

Numerical Analysis of Double-Diffusive Convection/Solidification Under *g*-Jitter/Magnetic Fields

K. Li* and B. Q. Li†
Washington State University, Pullman, Washington 99164
and
H. C. de Groh‡
NASA John H. Glenn Research Center at Lewis Field, Cleveland, Ohio 44135

A finite element model is presented for the *g*-jitter induced double-diffusive convection and solidification phenomena with and without the presence of magnetic fields in an Sn-doped Bi crystal growth system planned for space experiments. The model is developed based on the deforming finite element formulation with the penalty formulation for pressure approximation. An isothermal front tracking algorithm is used to predict the solid–liquid interface. Extensive numerical simulations are carried out and parameters studied include the solute concentration dependent melting temperature and magnetic field strength under both steady state and *g*-jitter conditions. Both synthesized *g*-jitter and real *g*-jitter data taken from space flights are used. Computed results show that the concentration effects on interface morphology must be considered for an accurate prediction of solidification interface morphology, and *g*-jitter can induce significant convective flows in the liquid pool, which, in turn, cause solute concentration nonuniformity during the space crystal growth. The use of an applied magnetic field can be effective in suppressing the deleterious *g*-jitter induced convection and solute nonuniformity and their effects on solidification.

Nomenclature

B_0	=	magnetic field magnitude
C	=	concentration
C_p	=	specific heat of Bi
C_0	=	solute concentration scale
D	=	solute diffusivity
$\mathrm{d}T/\mathrm{d}x$	=	temperature gradient
Gr_S	=	solutal Grashof number
Gr_T	=	thermal Grashof number
g_0	=	Earth gravity constant
H	=	latent heat of Bi
Ha	=	Hartmann number
$h(y)$	=	dimensionless x position of growth interface
$\hat{i}, \hat{j}$	=	unit vector of ith, jth component
k	=	thermal conductivity
k_0	=	segregation coefficient
L	=	length of three zones
L_c	=	length of cold zone
L_g	=	length of gradient zone
L_h	=	length of hot zone
L_0	=	dimensionless x position of hot end
L_1, L_4	=	dimensionless lower and upper y positions of ampoule outer surface
L_2, L_3	=	dimensionless lower and upper y position of ampoule inner surface
m	=	slope of solidus curve
$\hat{n}$	=	unit normal vector
Pr	=	Prandtl number
p	=	pressure
R_a	=	radiation number of ampoule
R_0	=	length scale
Sc	=	Schmidt number
Ste	=	Stefan number
T	=	temperature
T_c	=	cold zone temperature
T_h	=	hot zone temperature
T_m	=	dimensionless melting point
T_{m0}	=	melting temperature of pure Bi
T^*	=	dimensional temperature
t_0	=	timescale
U_0	=	velocity scale
$\boldsymbol{U}$	=	velocity vector
$\boldsymbol{U}^*$	=	interface velocity
u	=	x-direction velocity component
V_g	=	crystal pulling speed
V_p	=	dimensionless pulling speed
v	=	y-direction velocity component
W_i	=	inner width of ampoule
W_o	=	outer width of ampoule
β_C	=	solutal expansion coefficient
β_T	=	thermal expansion coefficient
ΔT	=	temperature scale
$\partial\Omega$	=	computational domain boundary
ε	=	penalty parameter for pressure
$\varepsilon_{\mathrm{amp}}$	=	blackbody coefficient of ampoule
κ	=	thermal diffusivity
ν	=	kinematic viscosity
ρ_0	=	density of pure Bi at T_m
σ_m	=	electrical conductivity
Ω	=	computational domain

Subscripts

amb	=	ambient
amp	=	ampoule
cry	=	crystal
i, j	=	ith, jth component

Superscipt

T	=	matrix transpose

Received 27 June 2002; revision received 6 December 2002; accepted for publication 9 December 2002.

*Research Associate, School of Mechanical and Materials Engineering.
†Professor, School of Mechanical and Materials Engineering; li@mme.wsu.edu.
‡Research Engineer.

I. Introduction

DIFFUSION-CONTROLLED melting crystal growth is possible when the intensity of convection in the liquid pool is negligible in comparison with atomic diffusion rate. In an idealized microgravity environment ($g = 10^{-6} g_0$), thermally induced convection is reduced to the level such that the diffusion-controlled growth is possible. This is indeed supported by some successful experiments on crystal growth in space. However, a majority of space-flight experiments suggest that space-grown crystals are inconsistent in quality and solute redistribution. Further examination of growth conditions and readings from accelerometers aboard the space vehicles reveals that the nonuniformity of solute distribution in these crystals is attributed to perturbed gravity forces, that is, g jitter.

A variety of sources may contribute to the gravity perturbations, which include crew motions, mechanical vibrations (pumps, motors, excitations of natural frequencies of spacecraft structures), spacecraft maneuvers and attitude, atmospheric drag, and the Earth's gravity gradient.[1] Signatures from the onboard accelerometers illustrate that g jitter is random in nature and varies in both direction and time. Although small, these perturbed forces can induce thermal convection that is strong enough to cause an unacceptable level of solute concentration nonuniformity in space grown crystals. Detailed studies have revealed that the g-jitter induced convection in spacecraft is directly related to the magnitude and frequency of the gravity perturbation and to the alignment of the gravity field with respect to the direction of the temperature gradient. The velocity attains a maximum when the gravity vector is perpendicular to the temperature gradients.[2–6]

Numerous numerical simulations have been conducted to understand and estimate the adverse effects of time-varying g jitter.[6–10] Both two- and three-dimensional numerical models have been developed for this purpose.[4,5,11] These models have been used to study the effects associated with both idealized single- and multiple-frequency g-jitter modulations and real g-jitter data collected by an accelerometer during actual flight experiments. These studies show that when the residual accelerations oscillate about the positive and negative of an axis, the orientation of this direction relative to the density gradient determines a mean flow in the system.[12] Sinusoidal accelerations induce an oscillating convective flow, which results in a composition variation in the liquid. Recently, Timchenko et al.[9] reported a study on the g-jitter influence of solute transport and convection together with solidification in a planned space-flight experiment. They used the finite difference approximation for field calculations and the enthalpy method to model the solid–liquid interface. In their calculations, the melting temperature of the pure solvent was used to determine the solid–liquid interface. They showed that, for large frequencies, higher amplitude of gravitational acceleration is required to produce effects on the segregation. Their study further illustrates that the concentration varies appreciably along the solid–liquid interface, suggesting that it is necessary to take into consideration the effects of concentration on the melting temperature to get an accurate estimate of the interface shape.

The use of a magnetic field to control the melt motion during single crystal growth has been widespread in the semiconductor industry. Studies on the g-jitter induced melt flows in the systems of relevance to space crystal growth experiments have been reported by Ma and Walker[11] and Baumgartl and Muller.[13] The former presented a semi-analytical model for the magnetic field effects on g-jitter driven thermal convection, whereas the latter presented a numerical model of melt flow driven by a single-frequency g-jitter force parallel to the thermal gradient with either transverse or axial fields imposed. Recently, Li and his coworkers[12,14–17] have reported a series of studies, including both analytical solutions and numerical simulations, on the magnetic field effects on the g-jitter induced flows and mass transfer. Their studies used both simulated g-jitter functions and real g-jitter data taken from typical space flights, with the latter intended to understand the thermal and flow phenomena in a realistic g-jitter environment. In space vehicles, g jitter is not aligned perfectly with the thermal gradient during crystal growth and the most deleterious flow effects come from the g-jitter component that is perpendicular to the thermal gradient.[4] The melt flow in microgravity is shown to have a very strong effect on the solute transport in typical space processing systems for crystal growth where the Schmidt number is large. Their studies further illustrate that these deleterious g-jitter effects can be suppressed by the application of an external magnetic field. Thus far, these studies have been primarily concerned with the convection with or without solute transport in the presence of magnetic fields, which is an idealized, though relevant, version of a melt growth furnace used for space flights. None of these studies have considered the solidification, which is a critical part of a crystal growth process. Nonetheless, these studies have provided a useful basis on which models incorporating more realistic considerations such as solidification and ampoule configuration, coupled with more realistic thermal boundary conditions, can be derived. These more realistic models will provide a much more useful tool, not only for enhancing our fundamental understanding of fluid mechanics and thermal phenomena in space crystal growth systems, but also for developing rational guidelines for both space experiment design and interpretation of experimental measurements.

In the present study, a finite element model is presented for the heat and mass transfer and solidification phenomena associated with the melt growth of single crystals in microgravity with and without an imposed magnetic field. The analysis is based on a two-dimensional geometry. Note that the furnace for the melt growth is of cylindrical geometry, and, under terrestrial conditions, a two-dimensional axisymmetric condition can be established. In a microgravity environment, however, such an axisymmetry condition cannot be maintained because the frequent maneuvering of space vehicles changes the gravity orientation constantly. Also note that because of the frequent change in gravity directions, in particular during the period when g jitter sets in, the flow structure is truly three-dimensional and three-dimensional models should be developed to fully appreciate the complex three-dimensional flow structure. Nonetheless, a two-dimensional analysis will provide some essential features of g-jitter induced flows and solidification behavior and help to develop fully three-dimensional models. The two-dimensional analysis presented hereafter is based on the solution of the transient Navier–Stokes equations for fluid flow, the energy balance equation for the temperature distribution, and the mass balance equation for species transport in an Sn-doped Bi alloy melt. The numerical scheme entails the implementation of a quasi-Lagrangian deforming finite element approach where the solid–liquid interface is tracked precisely by deforming the elements associated with the moving interface. Numerical results include the transient convective flows and solute redistribution in the melts and their effects on the solidification interface morphology under the combined action of g-jitter and external magnetic fields. Both synthetic g-jitter, which represents a single component of Fourier synthesis of g-jitter data, and the real g-jitter data, are used in the analyses.

II. Mathematical Formulation

Figure 1 schematically illustrates the two-dimensional model used to study the Bridgman Sn-doped Bi crystal growth in microgravity. An external dc magnetic field is applied along the thermal gradient. The ambient temperature profile T_{amb} consists of a cold zone T_c, a linear gradient zone $\mathrm{d}T/\mathrm{d}x$, and a hot zone T_h. The ampoule translation is simulated by feeding the melt with a uniform solute concentration C_0 into the inlet at the constant velocity V_g and pulling out the crystal from the outlet. The length of the computation domain is L, the inner width of the ampoule is W_i, and the outer width is W_o. The configuration described is similar to the two-dimensional model used by Yao et al.[18] to study the MEPHISTO Space Flight experiments.

In the preceding system, the time-dependent phenomena of fluid flow and heat and mass transfer with the presence of an applied magnetic field is described by the Navier–Stokes equations with the time-varying gravity force term and the Lorentz force term. The Boussinesq approximation, $\rho = \rho_0 \lfloor 1 - \beta_T (T^* - T_{m0}) + \beta_C (C - C_0) \rfloor$, is used. The nondimensional governing equations are given hereafter. For the melt,

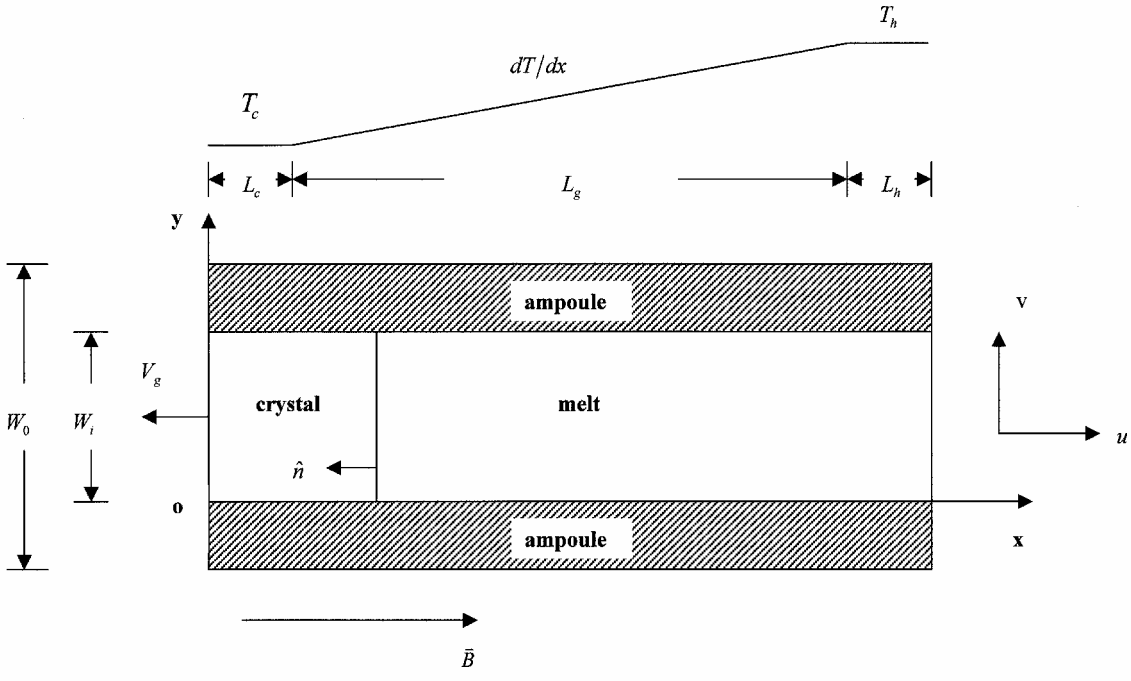

Fig. 1 Two-dimensional model for the Bridgman Sn-doped Bi space crystal growth system.

$$\nabla \cdot \boldsymbol{U} = 0 \tag{1}$$

$$\frac{\partial \boldsymbol{U}}{\partial t} + \boldsymbol{U} \cdot \nabla \boldsymbol{U} = -\nabla p + \nabla^2 \boldsymbol{U} + \boldsymbol{g}(t)[-Gr_T(T - T_m) + Gr_S(C - 1)] + Ha^2(\boldsymbol{U} \times \boldsymbol{B}) \times \boldsymbol{B} \tag{2}$$

$$\frac{\partial T}{\partial t} + \boldsymbol{U} \cdot \nabla T = \frac{1}{Pr}\nabla^2 T \tag{3}$$

$$\frac{\partial C}{\partial t} + \boldsymbol{U} \cdot \nabla C = \frac{1}{Sc}\nabla^2 C \tag{4}$$

The real g-jitter perturbation is random both spatially and temporally. In some cases, to help analyses, g jitter can be represented by the combination of a series of single-frequency accelerations, as follows:

$$\boldsymbol{g}(t) = \sum_{n=1}^{N} \boldsymbol{g}_n \sin(2\pi \omega_n t) \tag{5}$$

Here, $\boldsymbol{g}_n$ is the amplitude, and ω_n is the frequency associated with the nth component of g jitter. Both the synthetic and real g-jitter perturbations are considered here.

For the crystal and the ampoule, where a bulk flow is superimposed because of the choice of the coordinate system, only heat transfer analysis is needed. The solute diffusion in crystal is also ignored. With these simplifications, the governing equations can be written as follows:

$$\frac{\partial T_{\text{cry}}}{\partial t} + V_p(\hat{e}_x \cdot \nabla T_{\text{cry}}) = \frac{\kappa_{\text{cry}}}{\kappa}\frac{1}{Pr}\nabla^2 T_{\text{cry}} \tag{6}$$

$$\frac{\partial T_{\text{amp}}}{\partial t} + V_p(\hat{e}_x \cdot \nabla T_{\text{amp}}) = \frac{\kappa_{\text{amp}}}{\kappa}\frac{1}{Pr}\nabla^2 T_{\text{amp}} \tag{7}$$

In deriving the preceding equations, the following scales are used: $R_0 = 0.5W_i$ for length, $U_0 = \nu/R_0$ for velocity, $t_0 = R_0^2/\nu$ for time, $p_0 = \rho_0 U_0^2$ for pressure, C_0 for concentration, g_0 for gravity, B_0 for magnetic field, $\Delta T = (T_h - T_c)$ for temperature where the nondimensional temperature is $(T^* - T_c)/\Delta T$. Note that instead of ν, thermal diffusivity may be chosen to nondimensionalize the equations for this problem. The nondimensional parameters are defined as

$$Gr_T = \beta_T R_0^3 g_0 \Delta T \big/ \nu^2, \qquad Gr_S = \beta_c R_0^3 g_0 C_0 \big/ \nu^2$$

$$Pr = \nu/\kappa, \qquad Sc = \nu/D, \qquad R_a = \varepsilon_{\text{amp}} \sigma R_0 (\Delta T)^3 \big/ k_{\text{amp}}$$

$$V_p = V_g/U_0, \qquad Ste = H/\Delta T C_p, \qquad Ha = B_0 R_0 \sqrt{\sigma_m/\rho_0 \nu}$$

The boundary conditions for the configuration considered are determined by the physical constraints and are detailed hereafter.

For the melt, at $x = L_0$ and $L_2 \le y \le L_3$,

$$u = V_p, \qquad v = 0, \qquad T = 1$$

$$\hat{n} \cdot \nabla C = V_p Sc(C - 1)(\hat{n} \cdot \hat{e}_x) \tag{8}$$

At $h(y) \le x \le L_0$, $y = L_2$, and $y = L_3$,

$$u = V_p, \qquad v = 0, \qquad \hat{n} \cdot \nabla T = (k_{\text{amp}}/k)(\hat{n} \cdot \nabla T_{\text{amp}})$$

$$\hat{n} \cdot \nabla C = 0 \tag{9}$$

At $x = h(y)$ and $L_2 \le y \le L_3$,

$$\hat{n} \cdot (\boldsymbol{U} - \boldsymbol{U}^*) = \hat{n} \cdot \left(\boldsymbol{U}_{\text{cry}} - \boldsymbol{U}^*\right)$$

$$\hat{n} \times (\boldsymbol{U} - \boldsymbol{U}_{\text{cry}}) = 0, \qquad T = T_m + mC$$

$$\hat{n} \cdot \nabla C = Sc\left[\hat{n} \cdot (\boldsymbol{U} - \boldsymbol{U}^*)C - \hat{n} \cdot \left(\boldsymbol{U}_{\text{cry}} - \boldsymbol{U}^*\right)C_{\text{cry}}\right] \tag{10}$$

Along the solid–liquid interface,

$$(\hat{n} \cdot \nabla T) - (k_{\text{cry}}/k)(\hat{n} \cdot \nabla T_{\text{cry}}) = StePr\hat{n} \cdot \left(\boldsymbol{U}_{\text{cry}} - \boldsymbol{U}^*\right) \tag{11}$$

For the crystal, at $0 \le x \le h(y)$, $y = L_2$, and $y = L_3$,

$$\hat{n} \cdot \nabla T = (k_{\text{amp}}/k_{\text{cry}})(\hat{n} \cdot \nabla T_{\text{amp}}) \tag{12}$$

At $x = 0$, and $L_2 \le y \le L_3$,

$$T = 0 \tag{13}$$

For the ampoule, at $x = L_0$, $L_1 \le y \le L_2$, and $L_3 \le y \le L_4$,

$$T = 1 \tag{14}$$

At $0 \le x \le L_0$, $y = L_1$, and $y = L_4$,

$$\hat{n} \cdot \nabla T = -Ra\left[\left(T + T_c^*\right)^4 - \left(T_{\text{amb}} + T_c^*\right)^4\right] \tag{15}$$

At $x = 0$, $L_1 \le y \le L_2$, and $L_3 \le y \le L_4$,

$$T = 0 \tag{16}$$

where $T_c^* = T_c/\Delta T$, $C_{\text{cry}} = k_0 C$, $\hat{n} \cdot \boldsymbol{U}_{\text{cry}} = V_p$, and $\hat{n} \times \boldsymbol{U}_{\text{cry}} = 0$.

III. Method of Solution

The governing equations described, along with the boundary conditions, are solved using the deforming Galerkin finite element method. When the procedures in previous studies[16,17] are followed, the governing equations are recast in integral forms:

$$\left(\int_\Omega \psi \hat{i} \cdot \nabla \phi^T \, dV\right)\boldsymbol{U}_i = -\varepsilon\left(\int_\Omega \psi \psi^T \, dV\right)\boldsymbol{P} \tag{17}$$

$$\begin{aligned}
&\left(\int_\Omega \phi\phi^T \, dV\right)\frac{d\boldsymbol{U}_i}{dt} + \left(\int_\Omega \phi \boldsymbol{u} \cdot \nabla \phi^T \, dV\right)\boldsymbol{U}_i \\
&\quad - \left(\int_\Omega \hat{i} \cdot \nabla \phi \psi^T \, dV\right)\boldsymbol{P} + \left(\int_\Omega \nabla\phi \cdot \nabla\phi^T \, dV\right)\boldsymbol{U}_i \\
&\quad + \left[\int_\Omega (\hat{i} \cdot \nabla\phi)(\hat{j} \cdot \nabla\phi^T) \, dV\right]\boldsymbol{U}_j + \left(\int_\Omega \phi\theta^T \boldsymbol{g} \, dV\right)(\boldsymbol{T} - T_m) \\
&\quad - \left(\int_\Omega \phi\theta^T \boldsymbol{g} \, dV\right)(\boldsymbol{C} - 1) = \int_{\partial\Omega} \boldsymbol{n} \cdot \tau \cdot \hat{i}\phi \, dS \\
&\quad + \int_\Omega \phi Ha^2 (\boldsymbol{u} \times \boldsymbol{B} \times \boldsymbol{B}) \, dV
\end{aligned} \tag{18}$$

$$\begin{aligned}
&\left(\int_\Omega Pr\theta\theta^T \, dV\right)\frac{d\boldsymbol{T}}{dt} + \left(\int_\Omega Pr\theta \boldsymbol{u} \cdot \nabla\theta^T \, dV\right)\boldsymbol{T} \\
&\quad + \left(\int_\Omega \nabla\theta \cdot \nabla\theta^T \, dV\right)\boldsymbol{T} = -\int_{\partial\Omega} q_T \theta \, dS
\end{aligned} \tag{19}$$

$$\begin{aligned}
&\left(\int_\Omega Sc\theta\theta^T \, dV\right)\frac{d\boldsymbol{C}}{dt} + \left(\int_\Omega Sc\theta \boldsymbol{u} \cdot \nabla\theta^T \, dV\right)\boldsymbol{C} \\
&\quad + \left(\int_\Omega \nabla\theta \cdot \nabla\theta^T \, dV\right)\boldsymbol{C} = -\int_{\partial\Omega} q_c \theta \, ds
\end{aligned} \tag{20}$$

Once the forms of shape functions ϕ, ψ, and θ for velocity, pressure, and all remaining scalars are specified, the integrals defined in the preceding equations can be expressed in matrix form. Combining the momentum and energy equations into a single matrix equation gives rise to the following element stiffness matrix equation,

$$\begin{aligned}
&\begin{bmatrix} \boldsymbol{M} & 0 & 0 \\ 0 & \boldsymbol{N}_T & 0 \\ 0 & 0 & \boldsymbol{N}_C \end{bmatrix}\begin{bmatrix} \dot{\boldsymbol{U}} \\ \dot{\boldsymbol{T}} \\ \dot{\boldsymbol{C}} \end{bmatrix} \\
&\quad + \begin{bmatrix} \boldsymbol{A}(\boldsymbol{U}) + \boldsymbol{K} + \dfrac{1}{\varepsilon}\boldsymbol{E}\boldsymbol{M}_p^{-1}\boldsymbol{E}^T & \boldsymbol{B}_T & \boldsymbol{B}_C \\ 0 & \boldsymbol{D}_T(\boldsymbol{U}) + \boldsymbol{L}_T & 0 \\ 0 & 0 & \boldsymbol{D}_C(\boldsymbol{U}) + \boldsymbol{L}_C \end{bmatrix} \\
&\quad \times \begin{bmatrix} \boldsymbol{U} \\ \boldsymbol{T} \\ \boldsymbol{C} \end{bmatrix} = \begin{bmatrix} \boldsymbol{F} \\ \boldsymbol{G}_T \\ \boldsymbol{G}_C \end{bmatrix}
\end{aligned} \tag{21}$$

The integrated form of Eq. (11),

$$\begin{aligned}
&\left(\int_\Omega \theta\hat{n} \cdot \nabla\theta^T \, dV\right)\boldsymbol{T} - \left[\int_\Omega (k_{\text{cry}}/k)\theta\hat{n} \cdot \nabla\theta^T \, dV\right]\boldsymbol{T}_{\text{cry}} \\
&\quad = -\int_{\partial\Omega} q_T^* \theta \, dS
\end{aligned} \tag{22}$$

is applied as a surface energy source to the total thermal energy balance equation and added to the right-hand side of Eq. (21). Note that in constructing the preceding element matrix equation, the penalty formulation has been applied, and $\boldsymbol{P}$ in the momentum equation is replaced by $(1/\varepsilon)\boldsymbol{M}_p^{-1}\boldsymbol{E}^T\boldsymbol{U}$. The assembled global matrix equations are stored in the skyline form and solved using the Gaussian elimination method. The coefficient matrices of Eq. (21) are calculated by

$$\boldsymbol{M}_p = \int_\Omega \psi\psi^T \, dV, \qquad \boldsymbol{N}_T = \int_\Omega Pr\theta\theta^T \, dV$$

$$\boldsymbol{M} = \int_\Omega \theta\theta^T \, dV, \qquad \boldsymbol{N}_C = \int_\Omega Sc\theta\theta^T \, dV$$

$$\boldsymbol{E}_i = \int_\Omega \hat{i} \cdot \nabla\phi\psi^T \, dV, \qquad \boldsymbol{L}_C = \int_\Omega \nabla\theta \cdot \nabla\theta^T \, dV$$

$$\boldsymbol{L}_T = \int_\Omega \nabla\theta \cdot \nabla\theta^T \, dV, \qquad \boldsymbol{A}(\boldsymbol{U}) = \int_\Omega \phi\boldsymbol{u} \cdot \nabla\theta^T \, dV$$

$$\boldsymbol{D}_C(\boldsymbol{U}) = \int_\Omega Sc\theta\boldsymbol{u} \cdot \nabla\theta^T \, dV, \qquad \boldsymbol{D}_T(\boldsymbol{U}) = \int_\Omega Pr\theta\, \boldsymbol{u} \cdot \nabla\theta^T \, dV$$

$$\boldsymbol{B}_C = -\int_\Omega Gr_s(\boldsymbol{g}\phi\theta^T) \, dV, \qquad \boldsymbol{B}_T = \int_\Omega Gr_T(\boldsymbol{g}\phi\theta^T) \, dV$$

$$\boldsymbol{G}_C = -\int_{\partial\Omega} q_C\theta \, dS, \qquad \boldsymbol{G}_T = -\int_{\partial\Omega} q_T\theta \, dS$$

$$\begin{aligned}
\boldsymbol{F} = &\int_{\partial\Omega} \boldsymbol{n} \cdot \tau\phi \, dS + \int_\Omega \phi Ha^2(\boldsymbol{u} \times \boldsymbol{B} \times \boldsymbol{B}) \, dV \\
&+ \int_\Omega Gr_T(\boldsymbol{g}\phi\theta^T)T_m \, dV - \int_\Omega Gr_s(\boldsymbol{g}\phi\theta^T) \, dV
\end{aligned}$$

$$\boldsymbol{K}_{ij} = \left(\int_\Omega \nabla\phi \cdot \nabla\phi^T \, dV\right)\delta_{ii} + \int_\Omega (\hat{i} \cdot \nabla\phi)(\hat{j} \cdot \nabla\phi^T) \, dV$$

A quasi-Lagrangian deforming finite element approach is used to track the solute concentration dependent solidification interface accurately. By this method, the region that covers the solidifying liquid and solid is deformed, and the nodes within the region are allowed to move in accordance with the interface movement. These additional velocities that result from the mesh movement are added to the velocity field. Two basic algorithms can be applied. One treats the moving interface as a separate variable and the interface thermal boundary condition would then be incorporated into the global finite element matrix. The other treats the interface thermal boundary condition as a separate constraint and is solved separately from the coupled field equations. Our numerical experience shows that, in a majority of cases, the incorporation of the isothermal constraint into the global matrix results in a very unstable nonlinear system. The whole system is extremely sensitive to boundary perturbations, more often than not leading to divergence. Separation of the moving interface boundary coordinates from the global finite element field variable solutions requires the convergence of both moving interface coordinates and field variables in two related loops. For this case, the global finite element matrix has a smaller bandwidth and, thus, requires shorter CPU time for iteration of the field variables, which takes the majority of the computing time. Our tests further show that the two methods require approximately the same CPU time, with the latter being much more robust and numerically stable. Thus,

the latter has been used in the present study. There are also two different methods used to track the liquid–solid interface, which give the same results within the machine accuracy. One method entails the use of the weighted residual method to integrate the interface thermal boundary condition, $T = T_m + mC$, whereas the other uses a directional search of the melting temperature after the coupled thermal, solute, and fluid flowfield calculations have converged. The latter is adopted in the present study.

In summary, our interface tracking strategy used in the present study involves an iterative procedure that entails applying the energy balance equation along the interface as a surface source and searching for the interface position coordinates based on each converged field calculation. The updated interface positions are then fed back to the field calculations until both the interface position coordinates and field variables have converged to within a preset criterion.

IV. Results and Discussion

The finite element model described enables the prediction of steady and transient fluid flow, heat, and mass transfer and the solid–liquid interface morphology in single crystal growth systems under both terrestrial and microgravity conditions with and without the presence of a magnetic field in the axial direction. The model development was based on the modification of the finite element code that has been reported in early studies,[12,14–17] which includes both code development and benchmark testing for thermal and fluid flow calculations. The code for solidification and moving interface calculations was validated using both analytical solutions and experimental data, which will be in a future publication. The thermophysical properties and geometric dimensions for the study are given in Table 1. It is noted that $k_0 = 0.29$ at%/at% was used here to lessen the effects of solute at the interface and improve numerical stability. The results presented below used 2968 nine-node elements with an increasing mesh distribution near the interface. Tests were conducted to ensure that the numerical results are mesh-independent to within a tolerance of less than 1% (relative error) between two consecutively refined (node points doubled) meshes. Both the interface position and field variables have converged within a preset relative tolerance of 1×10^{-4}. Numerical simulations were carried out for a wide range of conditions, and a selection of the computed results is presented hereafter.

Table 1 Parameters used for calculations

Parameter	Value
	Physics properties
T_{m0}	544 K
ρ_0	10,070 kg m^{-3}
C_p	144.87 J kg^{-1}K^{-1}
ν	1.837×10^{-7} m^2 s^{-1}
D	2.7×10^{-9} m^2 s^{-1}
C_0	1 at%
β_T	1.25×10^{-4} K^{-1}
β_C	0.3049 (volume fraction)$^{-1}$
k_0	0.29 at%|at%
m	2.32 K|at%
g_0	9.8 ms^{-2}
H	5.25×10^4 J kg^{-1}
k	12.4 Wm^{-1} K^{-1}
k_{cry}	6.5 Wm^{-1} K^{-1}
k_{amp}	2.01 Wm^{-1} K^{-1}
κ	8.5×10^{-6} m^2 s^{-1}
κ_{cry}	4.5×10^{-6} m^2 s^{-1}
κ_{amp}	8.7×10^{-7} m^2 s^{-1}
ε_{amp}	0.8
	System parameters
W_i	6.0×10^{-3} m
W_o	1.0×10^{-2} m
L	4.2×10^{-2} m
L_h	4.95×10^{-3} m
L_c	4.95×10^{-3} m
L_g	3.21×10^{-2} m
dT/dx	2.0×10^4 Km^{-1}
T_h	973 K
T_c	323 K
V_g	-3.34×10^{-6} ms^{-1}
B_0	0.5 T
	Scale parameters
U_0	6.12×10^{-5} ms^{-1}
ΔT	650 K
R_0	3×10^{-3} m
t_0	49.0 s
	Nondimensional parameters
V_p	−0.055
T_c^*	0.497
Pr	0.0215
Sc	68.0
Gr_T	6.37×10^5
Gr_S	1.957×10^4
Ra	0.01859
T_m	0.34
Ste	0.558

A. Steady Microgravity Condition

When the space vehicle follows the orbit without disturbances, an idealized microgravity condition exists, which gives a gravity level of $10^{-6} g_0$. Numerical simulations were carried out for this condition without an imposed magnetic field. The results are useful in helping to gain physical insight into the steady-state behavior of the system, and they also provide the initial condition for the dynamic behavior of the system when g-jitter effects set in. The simulations were based on the direct numerical solution to the steady-state governing equations obtained by dropping out the time-dependent terms in the model equations described in Sec. II while keeping all of the mutually coupled terms. For this case, the gravity orientation is assumed to be perpendicular to the temperature gradient, which represents the worst-case scenario. The computed results show that the temperature distribution in the melt is mainly controlled by the thermal conduction. This is a direct result of small Prandtl number for the system being studied. Thus, the temperature distribution study is ignored thereafter. The thermal and solutal gradient induced flow is weak, and the flowfield is nearly dominated by the crystal growth velocity. The maximum velocity of the flowfield is 5.6×10^{-2}, which is slightly higher than the crystal pulling velocity of 5.5×10^{-2}. These results are qualitatively consistent with those obtained from a simplified crystal growth system where solidification was not considered.[17] The interface position, the melting temperature, and the solute concentration distribution along the interface are shown in Fig. 2. Clearly, the interface is concave into the solid phase, which is expected as the crystal loses heat through the two sides. Because of its dependency on solute concentration, the melting temperature is no longer constant along the interface, which results in a noticeable shift of the interface position. With a concave interface and with an absence of convection, the solute concentration along the interface would be nonuniform with a maximum at the center of the interface.[19,20] The effect of the tiny buoyant and solutal convection induced by microgravity is to skew this profile slightly toward $y = 2$. The solute concentration nonuniformity at the interface is about 7.1%, measured by $(C_{\max} - C_{\min})/C_{\text{average}}$ along the growth interface. This, together with other computed results, suggests that the dependency of melting temperature on solute concentration needs to be considered to predict the solidification interface positions accurately.

B. Single-Frequency g Jitter: Frequency Effects

Crystal growth experiments during space flights show that the frequency of g jitter has an important effect on the convection, solidification interface morphology, and the solute concentration in the melt pool. To investigate this effect, three g-jitter perturbation frequencies (0.01, 0.1, and 1 Hz) were studied, which cover the frequency range of practical importance to melt processing systems designed for space applications.[4,5,17] The same gravity magnitude ($10^{-3} g_0$) is used for all cases. The calculations were transient with the g-jitter force assuming a sinusoidal variation, and started from the steady-state conditions presented earlier as an initial condition.

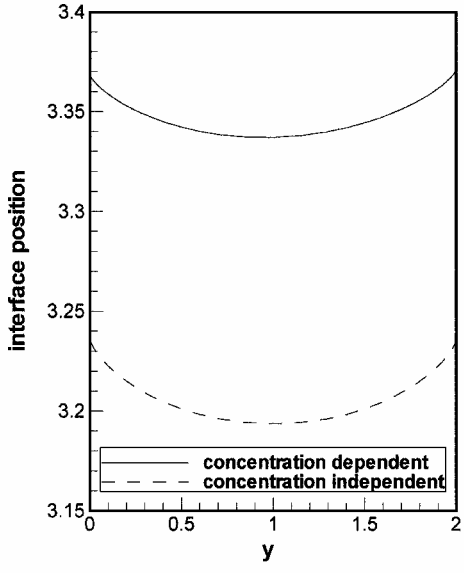

a)

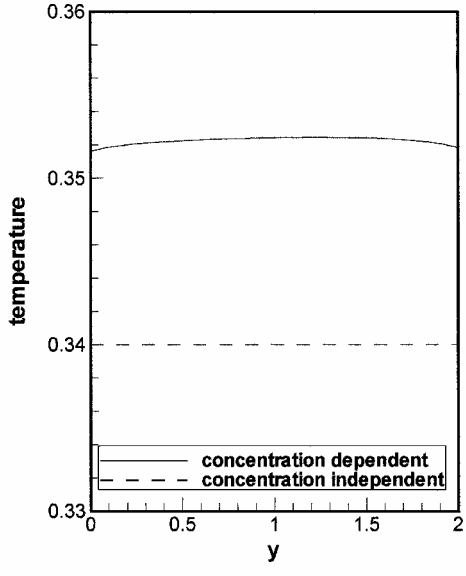

b)

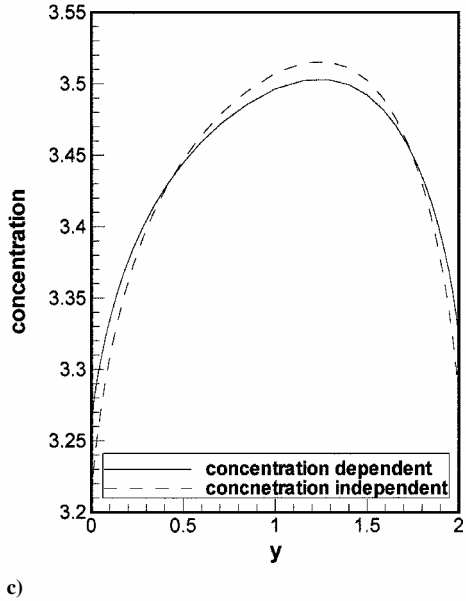

c)

Fig. 2 Solute concentration dependent a) interface position and b) melting temperature, and c) solute concentration distribution at the interface.

These were intended to simulate the situation in which a steady-state space growth condition is perturbed by gravity perturbations. The typical time evolutions of the field variables (u, v and C) near the solidification front are plotted in Fig. 3 for an elapse of 20 cycle periods of the corresponding g-jitter perturbations for all three different frequencies. It can be seen that, for all cases, the field variables oscillate at the same frequency of the driving g-jitter perturbations, and the oscillations eventually evolve to a time-harmonic quasi steady state. Examinations of detailed velocity field evolutions reveal that the convection loop in the melt pool oscillates and reverses its rotating direction at approximately the same frequency of the driving g-jitter force when the time harmonic quasi steady state is reached. The convection sweeps back and forth along the growth front and induces the solute concentration oscillation at the interface. Note that the oscillation magnitudes for the three cases are considerably different, although the same amplitude of the g-jitter perturbations was used for computations. The amplitudes of the velocity oscillation decrease dramatically, hence, the solute concentration oscillation, with an increase in frequency. Also, note that in Fig. 3c, the velocity oscillations experience approximately five irregular periods before reaching the quasi steady state, whereas those in Figs. 3a and 3b almost reach the quasi steady state over the first period. The solute concentration variations with time corresponding to the flow evolutions are also shown in Fig. 3. Clearly, as the frequency increases, the concentration variation decreases in response to the flow changes. For the present cases considered, at a frequency of 1 Hz, the concentration variation experiences an abrupt change over the transient period during which the flow reaches the quasi steady state. This is in contrast with the case at lower frequencies, say $f = 0.01$ and 0.1 Hz. The solute concentration continues to evolve after the flow reaches the quasi steady state for the three cases studied.

The flow oscillations have a significant influence on the solute concentration distribution, hence, the interface morphology. This is evident from Fig. 4, in which the interface shapes at the end of the same number of oscillation periods are depicted for the three cases considered. Clearly the strongest influence comes from the lower-frequency component, producing a significant deviation from the initial steady state. The deviation becomes smaller as the frequency increases. In particular, at $f = 1$ Hz, the interface shape remains basically unchanged. One of the important measures of single crystal qualities is the solute nonuniformity along the solid–liquid interface. Under g-jitter conditions, the solute concentration varies as a function of time. Figure 5 plots the time evolutions of the solute concentration nonuniformity, measured using $[C(t)_{\max} - C(t)_{\min}]/C(t)_{\text{average}}$ along the interface. It can be seen that for low-frequency component ($f = 0.01$ Hz), right after the g-jitter perturbations set in, the solute concentration nonuniformity increases significantly and oscillates with time. In fact, for the case considered, a sudden increase of about 40% in nonuniformity is initially observed, and this change gradually decreases, with the oscillation frequency nearly doubled at the end of 20 time periods. The effects become weaker with higher-frequency components. For the three cases studied, the nonuniformities are about 5–15% for $f = 0.01$ Hz and 8.7% for $f = 0.1$ Hz at the end of the 20 oscillation periods, respectively. The solute nonuniformity remains relatively unchanged with $f = 1$ Hz over the period of 20 cycles, with a concentration nonuniformity being around 7.1%. In combination with the results shown in Fig. 3, it is clear that the solute transport in the system is essentially convection dominant in that a strong oscillating convective flow near the solidification front causes a large nonuniformity in concentration. For the cases studied, such strong convection is attributed to the lower-frequency g-jitter perturbations, and, thus, eliminating this detrimental effect is crucial to produce crystals of desirable quality in space environments.

C. Combined Action of Single-Frequency g Jitter and Magnetic Fields

The idea of the use of magnetic fields to suppress the melt convection comes from an opposing Lorentz force arising from the interaction of the melt flow and an applied magnetic field. In the

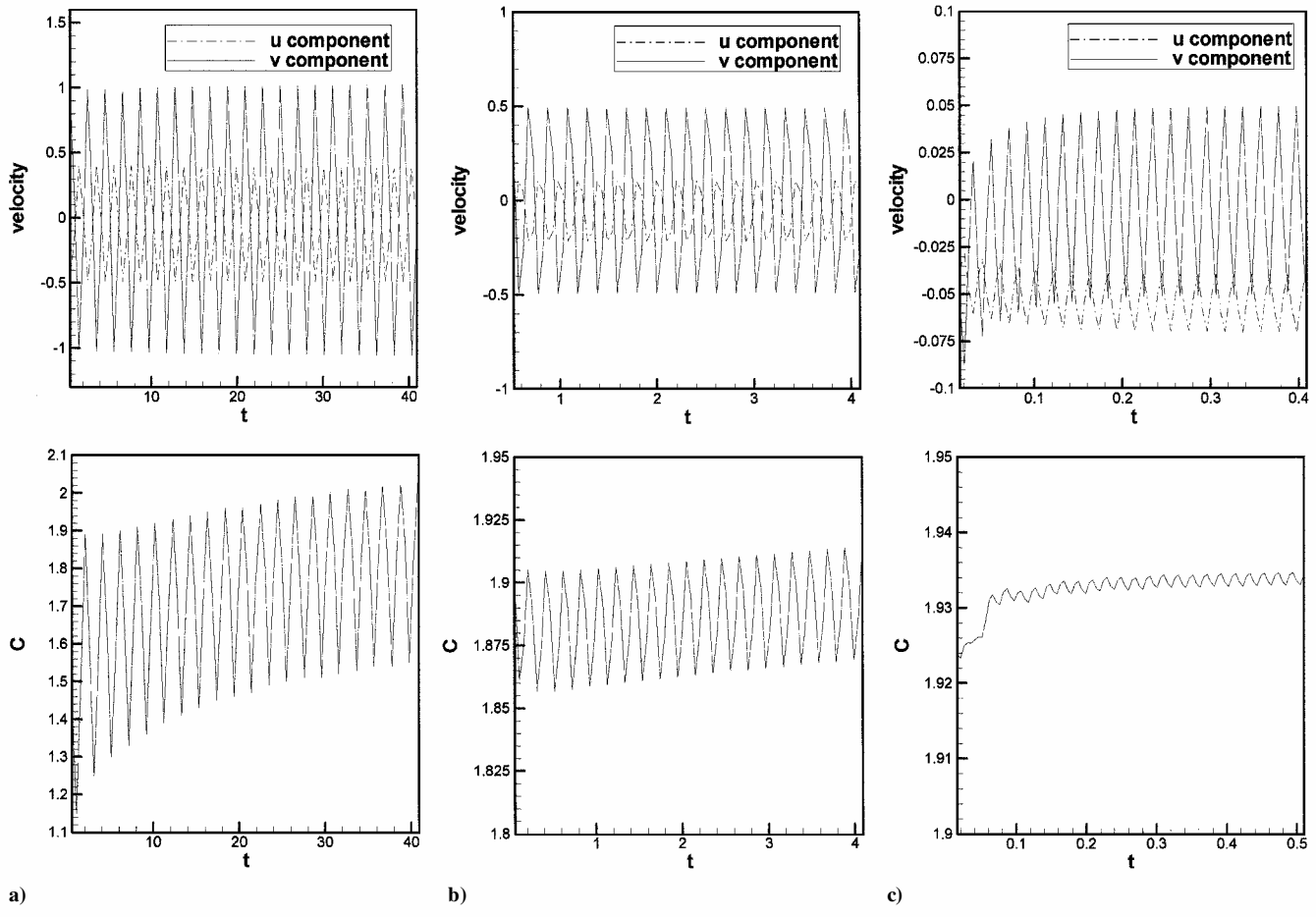

Fig. 3 Time evolutions of the velocities (upper) and the solute concentration (lower) at the position ($x = 3.6, y = 0.5$) caused by the single-frequency g-jitter perturbations with a) $f = 0.01$, b) 0.1, and c) 1 Hz.

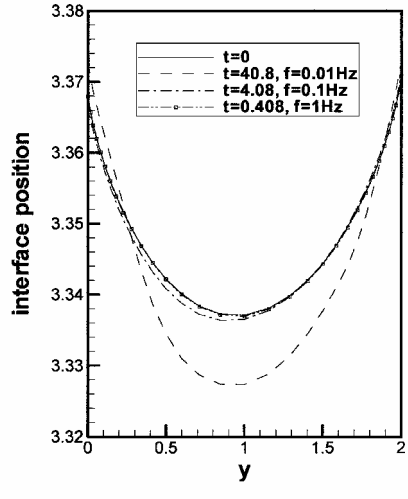

Fig. 4 Comparison of the interface positions at the same time period caused by the single-frequency g-jitter perturbations with $f = 0.01$, 0.1, and 1 Hz, respectively.

present study, the applied uniform dc magnetic field is aligned with the temperature gradient to suppress the flow along the interface. The applied magnetic field strengths are 0.1 ($Ha = 7.7$), 0.3 ($Ha = 23.2$) and 0.5 T ($Ha = 38.7$). The single-frequency (0.1-Hz) g-jitter perturbation is used here. The calculations assumed that the magnetic field is switched on at the same time g jitter sets in. The computed results for the time development of the field variables (u, v, and C) are plotted in Fig. 6. Figure 6 shows that the magnetic fields can effectively reduce the magnitudes of the field variable variations, and the magnetic damping effect becomes stronger with an increase in the applied magnetic field strength. However, the magnetic fields do not affect the frequency of the field variable oscillations. Further examination of the flowfields shows that with a moderate magnetic strength (0.5 T, $Ha = 38.7$), a factor of four in velocity reduction is achieved for the present system and the convection cell is limited in the central region of the liquid pool. For example, at time $t = 4.0902$, the maximum velocities of the flowfield are $U_{max} = 0.616$ ($Ha = 0$), $U_{max} = 0.560$ ($Ha = 7.7$), $U_{max} = 0.406$ ($Ha = 23.2$), and $U_{max} = 0.160$ ($Ha = 38.7$), respectively.

Figure 7 illustrates the interface morphology and the solute concentration distributions along the interface at $t = 4.0902$. It can be seen that, with an applied magnetic field, the g-jitter induced interface deviation from that of the steady microgravity case is reduced significantly, and so is the solute concentration nonuniformity along the interface, as a result of reduction in convection in the melt. With a magnetic field strength of 0.5 T ($Ha = 38.7$), the deviation between the interface shape affected by the g-jitter perturbation and the steady microgravity condition is suppressed almost completely. This is also consistent with the reduction of the solute concentration nonuniformity along the interface in the presence of the magnetic fields, as depicted in Fig. 7c. Here, it is clear that the solute concentration nonuniformities decrease dramatically with the increasing magnetic field strength. With a magnetic field strength of 0.5 T ($Ha = 38.7$), the solute concentration nonuniformity caused by the g-jitter perturbation is smoothed out almost entirely. Numerical calculations were also done with other frequencies and the same conclusions held. The results suggest that a strong magnetic field can be used to effectively suppress the detrimental effects caused by the g-jitter induced convection on the solute distribution in the space-grown crystals.

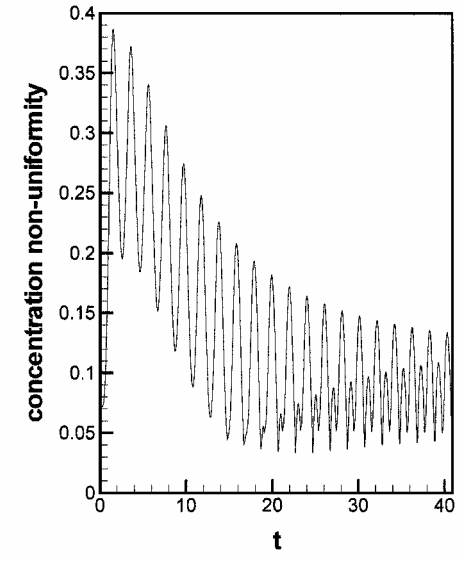

a)

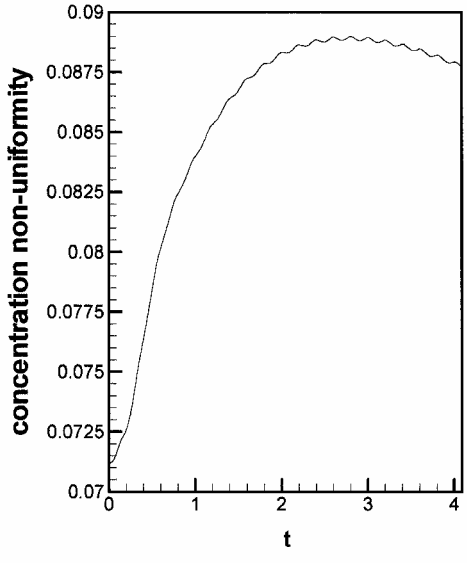

b)

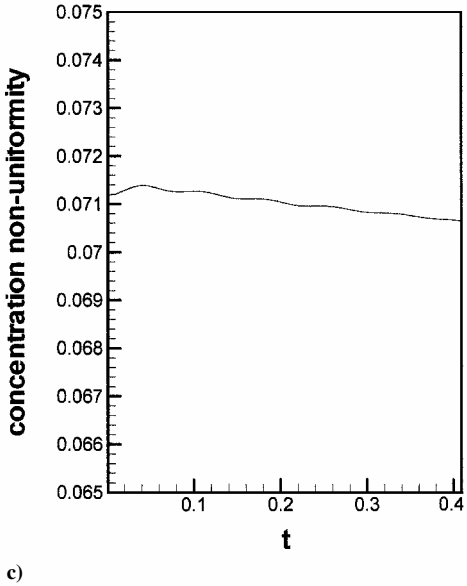

c)

Fig. 5 Time evolutions of the solute concentration nonuniformity measured by $[C(t)_{max} - C(t)_{min}]/C(t)_{average}$ at the interface caused by the single-frequency g-jitter perturbations with a) $f = 0.01$, b) 0.1, and c) 1 Hz.

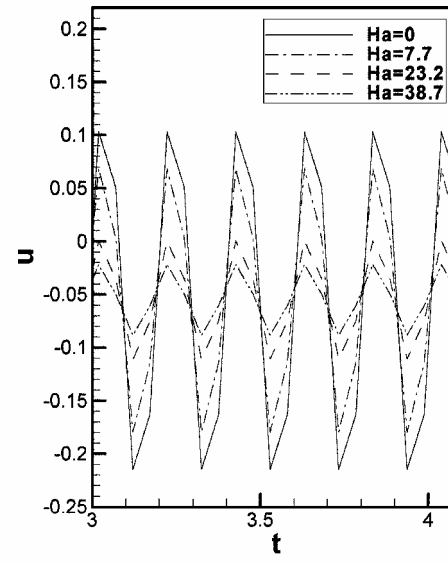

a)

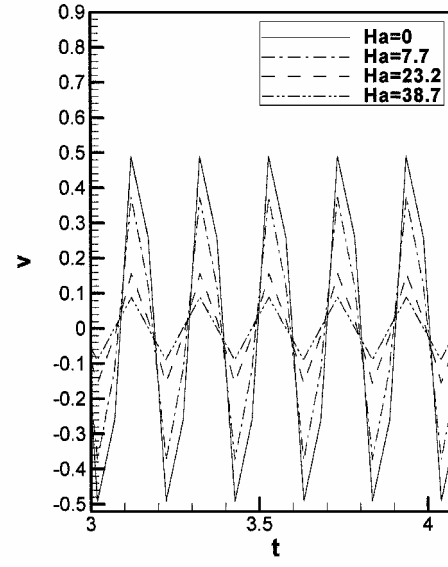

b)

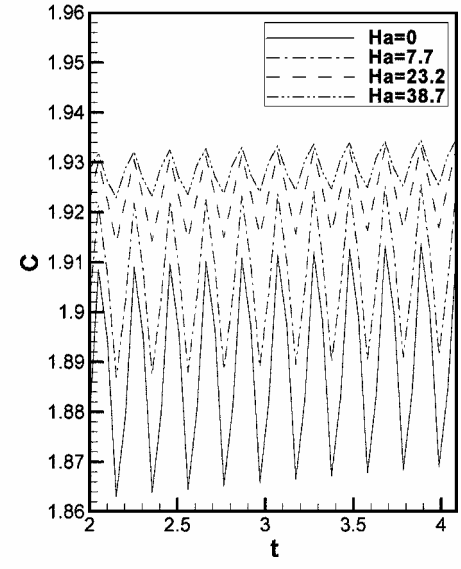

c)

Fig. 6 Effects of the magnetic field intensities on the time evolutions of velocities and solute concentration at the position $(x = 3.6, y = 0.5)$ caused by the single frequency ($f = 0.1$ Hz) g-jitter perturbation.

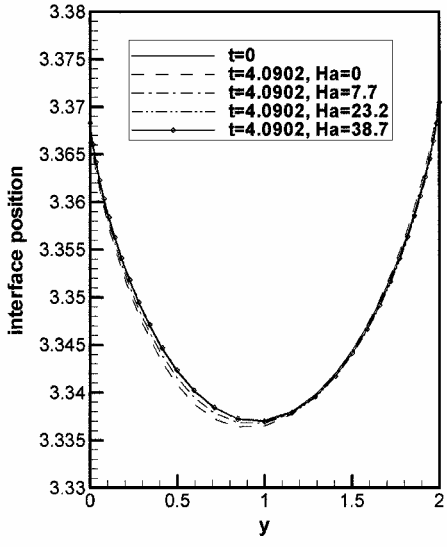

a)

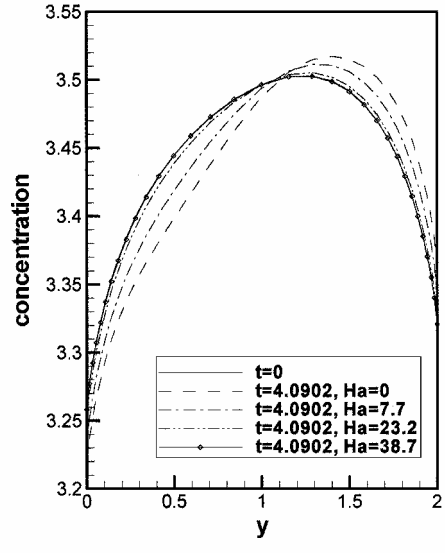

b)

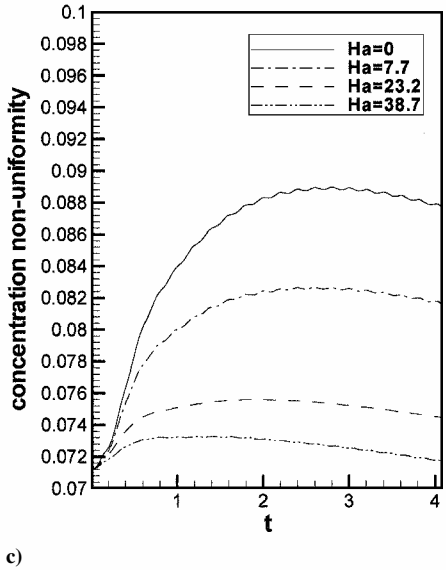

c)

Fig. 7 Effects of the magnetic field intensities on a) the interface positions, b) the solute concentration distributions at the interface at $t = 4.0902$, and c) the time evolutions of the solute concentration nonuniformity measured by $[C(t)_{\max} - C(t)_{\min}]/C(t)_{\text{average}}$ at the interface caused by the single frequency ($f = 0.1$ Hz) g-jitter perturbation.

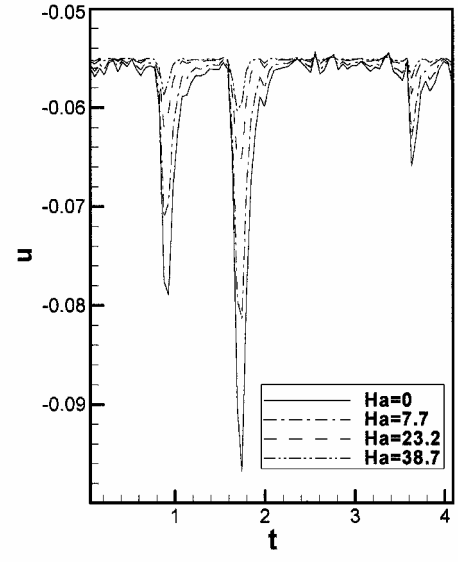

a)

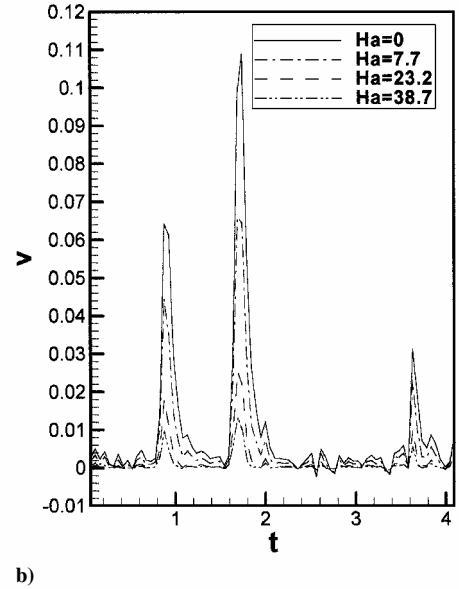

b)

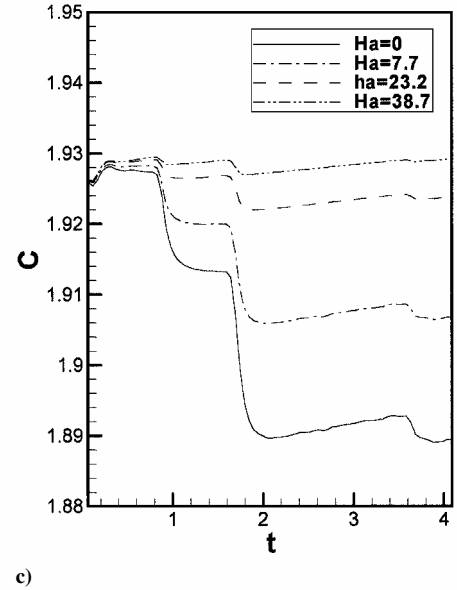

c)

Fig. 8 Effects of the magnetic field intensities on the time evolutions of velocities and solute concentration at the position ($x = 3.6, y = 0.5$) caused by the real g-jitter perturbation.

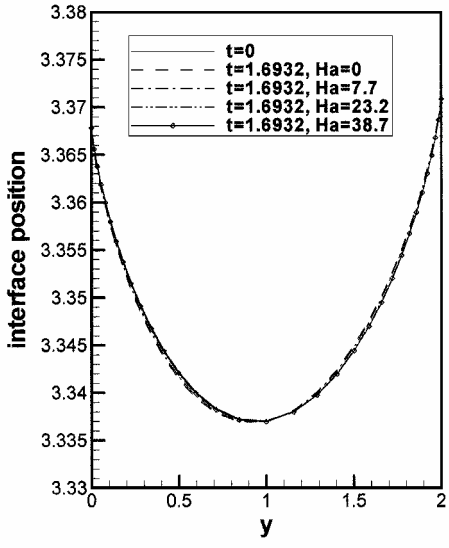

a)

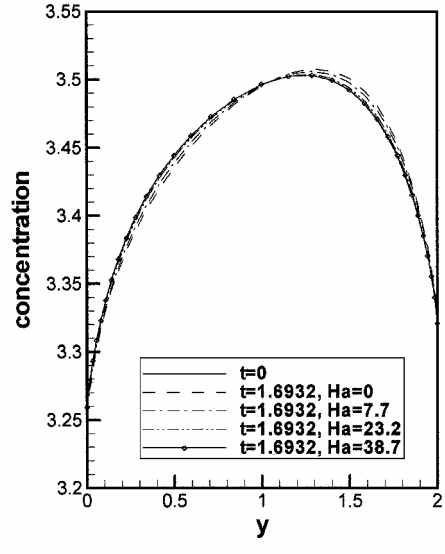

b)

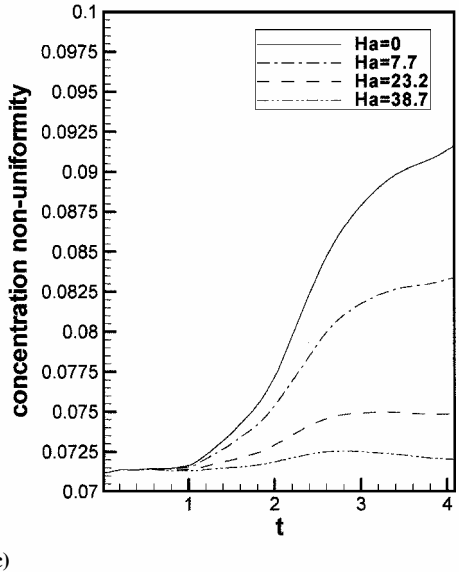

c)

Fig. 9 Effects of the magnetic field intensities on a) the interface positions, b) the solute concentration distributions at the interface at $t = 1.6932$, and c) the time evolutions of the solute concentration nonuniformity measured by $[C(t)_{max} - C(t)_{min}]/C(t)_{average}$ at the interface caused by the real g-jitter perturbation.

D. Combined Action of Real g Jitter and Magnetic Fields

Although the studies on the single-frequency effects are of great importance in helping to understand the fundamentals governing the thermally induced oscillating flows in space, information on the heat and mass transfer in a real space environment is of both theoretical and practical significance. Numerical simulations were carried out using the real g-jitter perturbation taken from the accelerometers aboard on a space flight. The data were given in an earlier publication[17] and are therefore, omitted here. Here again, the computations assume that the magnetic fields are switched on when the g jitter becomes effective. Figure 8 compares the time evolutions of field variables (u, v, and C) in the melt induced by g-jitter signatures with and without the applied magnetic fields. It can be seen that the velocity oscillations are random in amplitude with time. The variation patterns are very similar to those of the real g-jitter perturbation. In all cases, the three main velocity spikes are caused by the sudden amplitude increases of the g-jitter perturbation. These spikes are responsible for the large amplitude jumps in the time evolution of the solute concentration (Fig. 8c), whence the defects are incorporated into the crystals in a random fashion. Figure 8 also clearly indicates that the magnetic fields can effectively suppress the velocity variations in a real g-jitter environment, especially for those large-amplitude velocity spikes. With a magnetic field strength of 0.5 T ($Ha = 38.7$), the solute concentration spikes due to g-jitter induced convections are eliminated almost entirely (Fig. 8c). The effects of the magnetic field intensities on the interface shapes and the solute concentration distribution at the interface at the time ($t = 1.6932$) when the highest velocity spike appears are shown in Figs. 9a and 9b. Note that the magnetic fields reduce the solute concentration deviation from that of the steady microgravity case. The effects of the magnetic field intensities on the time variations of the solute concentration nonuniformities along the interface are shown in Fig. 9c. Inspection of these results indicates that the real g-jitter perturbation can significantly increase the solute concentration nonuniformity and that this sharp rise in concentration nonuniformity can be substantially suppressed by an applied magnetic field. Note that with a moderate magnetic field (0.5 T), the extra solute concentration non-uniformity caused by the real g-jitter perturbation is almost entirely smoothed out. These results demonstrate that an appropriate magnetic field can be applied to control effectively the field variations and solute concentration nonuniformity caused by g-jitter perturbations in space processing systems.

V. Conclusions

A transient two-dimensional numerical model has been presented for convection and solidification under the combined influence of g-jitter perturbations and an applied magnetic field. The model has been developed based on the solution of transient magnetohydrodynmaic equations with allowance for both heat and mass transfer and with the deforming finite element methodology to track the moving solid–liquid interface. The model is capable of predicting the phenomena of steady-state and transient heat and mass transfer, solute distribution, and the solidification interface associated with the crystal growth in microgravity with and without an applied magnetic field. Numerical simulations were carried out under the idealized microgravity condition, the synthesized g-jitter perturbations, and real g-jitter perturbations taken by onboard accelerometers during a space flight. Computed results demonstrate that g jitter can cause significant convective flows in the liquid pool, which, in turn, induce large solute concentration nonuniformity during the melt growth of single crystals in space. An applied magnetic field can be very effective in suppressing the detrimental effects on convection and solute concentration nonuniformity caused by the g-jitter perturbations. Consequently, a diffusion-controlled growth environment is possible with a combination of microgravity and an applied magnetic field.

Acknowledgment

The financial support of this work by the NASA Microgravity Science and Application Division (Grant NAG8-1693) is gratefully acknowledged.

References

[1]Alexander, J. I. D., "Low-Gravity Experiment Sensitivity to Residual Acceleration: A Review," *Microgravity Science and Technology*, Vol. 2, No. 3, 1994, pp. 131–135.

[2]de Groh, H. C., III, and Nelson, E. S., "On Residual Acceleration During Space Experiments," *ASME Winter Annual Meeting*, HTD-Vol. 290, American Society of Mechanical Engineers, Fairfield, NJ, 1994, pp. 23–33.

[3]Schneider, S., and Straub, J., "Influence of the Prandtl Number on Laminar Natural Convection in a Cylinder Caused by *g*-Jitter," *Journal of Crystal Growth*, Vol. 97, No. 1, 1989, pp. 235–242.

[4]Alexander, J. I. D., Quazzani, J., and Rosenberger, F., "Analysis of the Low Gravity Tolerance of the Bridgman–Stockbarger Crystal Growth I: Steady and Impulse Accelerations," *Journal of Crystal Growth*, Vol. 97, No. 1, 1989, pp. 285–302.

[5]Alexander, J. I. D., Amiroudine, S., Quazzani, J., and Rosenberger, F., "Analysis of the Low Gravity Tolerance of the Bridgman–Stockbarger Crystal Growth II: Transient and Periodic Accelerations," *Journal of Crystal Growth*, Vol. 113, Nos. 1–2, 1991, pp. 21–38.

[6]Zhang, W., Casademunt, J., and Venals, J., "Study of Parametric Oscillator Driven by Narrow-band Noise to Model the Response of a Fluid Surface to Time-Dependent Acceleration," *Physics of Fluids*, Vol. 5, No. 12, 1993, pp. 3147–3161.

[7]Wheeler, A. A., Mcfadden, G. B., Murray, B. T., and Coriell, S. R., "Convection Stability in Rayleigh-Benard and Directional Solidification Problems: High Frequency Gravity Modulation," *Physics of Fluids*, Vol. 3, No. 12, 1991, pp. 2847–2853.

[8]Benjapiyaporn, C., Timchenko, V., Leonardi, E., Davis, G., de Vahl, and de Groh, H. C., III, "Effects of Space Environment on Flow and Concentration During Directional Solidification," NASA TM 209293, 2000.

[9]Timchenko, V., Chen, P. Y. P., Leonardi, E., Davis, G., de Vahl, and Abbaschian, R., "A Computational Study of Transient Plane front Solidification of Alloys in a Bridgman Apparatus Under Microgravity Conditions," *International Journal of Heat and Mass Transfer*, Vol. 43, No. 6, 2000, pp. 963–980.

[10]Series, R. W., and Hurle, D. T. J., "The Use of Magnetic Field in Semiconductor Crystal Growth," *Journal of Crystal Growth*, Vol. 113, Nos. 1–2, 1991, pp. 305–328.

[11]Ma, N., and Walker, J. S., "Magnetic Damping of Buoyant Convection During Semiconductor Crystal Growth in Microgravity: Spikes on Residual Acceleration," *Physics of Fluids*, Vol. 8, No. 4, 1996, pp. 944–949.

[12]Pan, B., and Li, B. Q., "Effects of Magnetic Field on Oscillating Mixed Convection," *International Journal of Heat and Mass Transfer*., Vol. 41, No. 16, 1998, pp. 2705–2710.

[13]Baumgartl, J., and Muller, G., "The Use of Magnetic Fields for Damping the Action of Gravity Fluctuations (*g*-Jitter) During Crystal Growth Under Microgravity," *Journal of Crystal Growth*, Vol. 169, Nos. 1–4, 1996, pp. 582–586.

[14]Shu, Y., Li, B. Q., and de Groh, H. C., III, "Magnetic Damping of *g*-Jitter Induced Double Diffusive Convection in Microgravity," *Numerical Heat Transfer*, Vo1. 42, No. 4, 2002, pp. 345–364.

[15]Handa, J., Zhang, X., Li, B. Q., and de Groh, H. C., "A 3-D Model for Magnetic Damping of *g*-Jitter Induced Convection and Solutal Transport in a Simplified Bridgman Configuration," *Proceedings of the ASME Heat Transfer Division*, American Society of Mechanical Engineers, Fairfield, NJ, 2001, HTD-24291, pp. 1–18.

[16]Song, S. P., and Li, B. Q., "A Hybrid Boundary/Finite Element Method for Simulating Viscous Flows and Shapes of Droplets in Electric Fields," *International Journal of Computational Fluid Dynamics*, Vol. 15, No. 1, 2002, pp. 293–308.

[17]Pan, B., Shang, D. Y., Li, B. Q., and de Groh, H. C., III, "Magnetic Damping Effects on *g*-Jitter Driven Melt Convection and Mass Transfer in Microgravity," *International Journal of Heat and Mass Transfer*, Vol. 45, No. 1, 2002, pp. 125–144.

[18]Yao, M. W., Raman, R., and de Groh, H. C., III, "Numerical Simulation of Heat and Mass Transport During Space Crystal Growth With MEPHISTO," NASA TM 107015, 1995.

[19]Coriell, S. R., and Sekerka, R. F., "Lateral Solute Segregation During Unidirectional Solidification of a Binary Alloy with a Curved Solid–Liquid Interface," *Journal of Crystal Growth*, Vol. 46, No. 1, 1979, pp. 479–482.

[20]Coriell, S. R., and Sekerka, R. F., "Lateral Solute Segregation During Unidirectional Solidification of a Binary Alloy with a Curved Solid–Liquid Interface: II. Large Departures from Planarity," *Journal of Crystal Growth*, Vol. 54, No. 1, 1981, pp. 167–175.